Peer Reviewed Paper openaccess

Reflectance spectra and AVIRIS-NG airborne hyperspectral data analysis for mapping ultramafic rocks in igneous terrain

K. Tamilarasan,[a] S. Anbazhagan,[a,*] S. Uma Maheswaran,[a] S. Ranjithkumar,[a] K.N. Kusuma[b] and V.J. Rajesh[c]

[a]Centre for Geoinformatics and Planetary Studies, Periyar University, Salem-636011, India
[b]Department of Earth Sciences, Pondicherry University, Puducherry, India
[c]Department of Earth and Space Sciences, Indian Institute of Space Science and Technology, Tiruvananthapuram, India

Contacts
K. Tamilarasan: ktamilarasan05@gmail.com
https://orcid.org/0000-0001-5880-4093
S. Anbazhagan: anbu02@gmail.com
https://orcid.org/0000-0003-3366-1895
S. Uma Maheswaran: umamahes05@gmail.com
S. Ranjithkumar: georanjith1993@gmail.com
https://orcid.org/0000-0001-9727-2309
K.N. Kusuma: kusuma.kn@gmail.com
V.J. Rajesh: rajeshvj@iist.ac.in

The layered Sittampundi Anorthosite Complex is covered by mafic and ultramafic rocks including anorthosite, gabbro, pyroxenite and other igneous rocks. The ultramafic terrain has frequently undergone metamorphism. In the present study, laboratory spectral measurements were carried out from mafic, ultramafic and felsic rocks in the 350–2500 nm spectral range to characterise their diagnostic spectral features and for further utilisation for rock-type mapping. In 2016, the Sittampundi complex was covered by an AVIRIS-NG airborne survey jointly conducted by the Space Application Centre (SAC-ISRO) and Jet Propulsion Laboratory (NASA). The level-2 AVIRIS-NG data was obtained from SAC and used to interpret various rock types. ENVI 5.3 software was used for digital image processing of the AVIRIS-NG airborne hyperspectral data. The continuum-removed spectra of major rock types including anorthosite, meta-anorthosite, gabbro, meta-gabbro, pyroxenite, pegmatite, granite, gneiss and migmatite were critically analysed and their diagnostic absorption features correlated with chemistry and mineralogy. The AVIRIS-NG data analyses include bad band removal, minimum noise fraction transformation (MNF) and band combination. Out of various band combinations, the MNF composite images B456, B546 and B561 provided an enhanced output for the delineation of various rock types in the ultramafic terrain.

Keywords: ultramafic terrain, Sittampundi, reflectance spectra, AVIRIS-NG, anorthosite

Introduction

Hyperspectral remote sensing is a rapidly growing technology, especially in the last three decades. It is also referred to as imaging spectrometry. Hyperspectral data have been available since 1983, however, the technology has only been widely used in recent times, because of the involvement of complicated factors such as sensor correction, atmospheric error, availability of suitable software and trained manpower.[1] Hyperspectral sensors offer

Correspondence
S. Anbazhagan: anbu02@gmail.com

Received: 27 April 2022
Revised: 5 September 2022
Accepted: 7 October 2022
Publication: 19 October 2022
doi: 10.1255/jsi.2022.a9
ISSN: 2040-4565

Citation
K. Tamilarasan *et al.*, "Reflectance spectra and AVIRIS-NG airborne hyperspectral data analysis for mapping ultramafic rocks in igneous terrain", *J. Spectral Imaging* **11**, a9 (2022).
https://doi.org/10.1255/jsi.2022.a9

a unique combination of both spectrally and spatially contiguous images that allow the accurate mapping of minerals and rock bodies.[2] The high-quality geological mapping required to adopt hyperspectral remote sensing provides the potential to conduct previously unimagined levels of geological mapping and exploration.[3] Imaging spectroscopy has become a vital tool for remote compositional assessment of terrestrial as well as planetary bodies.[4,5] In this context, reflectance spectral studies were carried out to characterise lunar analogue material.[6,7] The high-resolution spectral data obtained through imaging spectrometers allow direct identification of materials based on their reflectance characteristics.[1,2,8–16] Several workers have evaluated the high-resolution airborne imaging spectrometer for mapping mineralogical variations and correlated absorption features with various mineral compositions.[8,17–19]

In comparison with multispectral data analysis in lithological mapping,[20] the hyperspectral remote sensing technique is more useful in geology, because a lot of minerals have diagnostic absorption features in the electromagnetic radiation spectrum.[21] Quite a number of researchers have applied hyperspectral remote sensing for the discrimination of minerals and lithological mapping.[2,22–25] Ramakrishnan and Bharti[26] reviewed the potential application of hyperspectral remote sensing techniques for geological applications. Magendran and Sanjeevi[27] differentiated grades of iron ore through absorption band centres extracted from Hyperion data. They correlated the percentage of iron ore oxide with the near infrared (NIR) absorption features. Paramasivam and Anbazhagan[28] utilised ASTER satellite data for the mapping of ultramafic rocks and ore minerals. Kruse[29] utilised AVIRIS data for geological study in the Colorado Plateau, southern San Juan County which lies in south-east Utah.

In the last two decades, rock-type discrimination and mapping of the mineralised zones has been carried out with the help of airborne hyperspectral data like AVIRIS, HYDICE, DAIS, HyMAP and the spaceborne sensor Hyperion data.[22,30–32] There are several spaceborne hyperspectral remote sensing data sets available at present. The major setback in the acceptance of hyperspectral data usage is the lack of high-quality data sets for most areas.[33] The gap has been replaced with a high-quality hyperspectral sensor available with AVIRIS-NG airborne data. In this context, the AVIRIS-NG data has been successfully applied in the fields of ecology and the environment.[34,35]AVIRIS-NG hyperspectral data is widely utilised in the field of geology and exploration of potential economic minerals. Oommen and Chatterjee[36] have adopted AVIRIS-NG spectral data for rock-type discrimination and mineral mapping using automated mapping techniques in the area of the Hutti–Maski greenstone belt, India. Bhattacharya *et al.*[37] utilised AVIRIS-NG data for mapping of the Jahazpur mineralised belt, Ambaji polymetallic sulfide and chromitite exposure of Sittampundi in India.

In 2016, the Space Application Centre (ISRO) successfully conducted an airborne hyperspectral imaging campaign with the help of JPL Laboratory, NASA/USA. Through this joint venture, the AVIRIS-NG instrument was flown over various parts of India and covered specific areas for different applications such as geology, forestry, agriculture, urban, glaciers, coastal and backwater environments. AVIRIS-NG has 5 nm spectral resolution within the wavelength range of 380–2510 nm. During the first phase of the campaign, AVIRIS-NG data were collected from the Sittampundi Anorthosite Complex, a geologically important terrain located in the southern part of India. The objective of the present study is to analyse the AVIRIS-NG airborne hyperspectral data and laboratory reflectance spectral data for the discrimination of various rock types in the ultramafic terrain. In addition, mineralogical and chemical studies were carried out to supplement and characterise the spectral data.

Location and geological setting

The Sittampundi Anorthosite Complex is located in Namakkal District in the southern part of India (Figure 1). The multiple folded, poorly exposed layered anorthosite complex is spread over a strike length of about 23 km. Subramaniam[38] studied the Sittampundi Anorthositic Complex in detail and documented the terrain as a metamorphosed igneous complex. In addition, several researchers explored the Sittampundi Anorthosite Complex and studied the origin of layered anorthosite, petrology, chronology, metamorphism and economic mineral deposits in the complex.[39–47] The layered anorthositic body is part of the southern granulite terrain of south India and is located in the Moyar–Bhavani–Cauvery tectonic zone. The study area belongs to the Archean age with a period of 2935 ± 60 Ma.[48] The major rock types in the anorthosite complex are anorthosite, meta-anorthosite, gabbro and pyroxenite (Figure 1). The other rock types in the Sittampundi complex are lenses of chromitite, garnet–pyroxene rocks (ecologites), hornblendite, peridotite, pegmatite and anthophyllite.[44] The anorthosite formation is bounded by quartzo feldspathic hornblende biotite gneiss, granitic gneiss and migmatites.

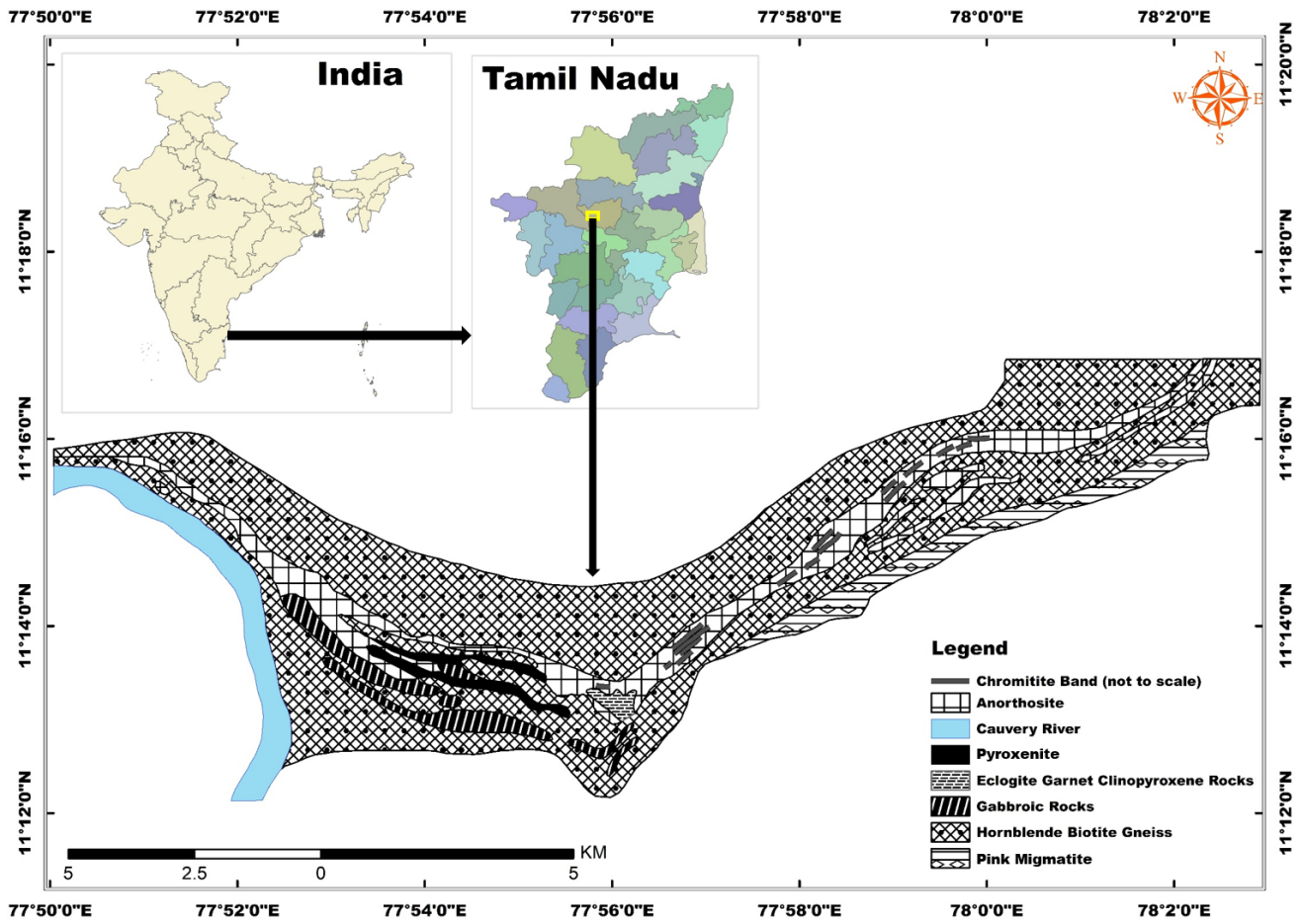

Figure 1. Location and geology map of Sittampundi ultramafic terrain, Tamil Nadu, India.[50]

Anbazhagan and Arivazhagan[6] have studied the spectra, chemistry and mineralogy of Sittampundi anorthosites, which are considered an equivalent of the anorthosites present in the lunar highland region. The presence of high calcic plagioclase in anorthosite is an important criterion to categorise Sittampundi anorthosite as an analogue for the lunar highland crust. The anorthosites in Sittampundi are relatively dominated by pure calcic anorthite (An 82-100) with less than 10% of mafic minerals.[6,44] Arivazhagan and Anbazhagan[49] utilised Landsat7 ETM multispectral satellite data and ASTER data for mapping rock types of the anorthosite complex. The multispectral remote sensing data provide broad spectral signatures for anorthosites in the study area.

Materials and methods

Reflectance spectral studies

The spectra of rocks and minerals are considered a basic input for understanding and assessing the possibility of airborne and spaceborne hyperspectral remote sensing data used in geoscience.[21] Reflectance spectroscopic studies are useful to identify the minerals with the help of diagnostic absorption features in the spectra. Hunt[51] has done detailed studies to characterise the diagnostic spectral features of minerals in the visible, NIR and mid-infrared spectral ranges. The diagnostic spectral characteristics of different minerals and rocks in a specific spectral range permit us to access their composition and relative abundance.[53] Absorption features such as absorption band centre, absorption width, symmetry and absorption depth provide valuable information for the identification and mapping of minerals and rocks from the continuum-removed spectra. In the last three decades, geoscientists have successfully adopted the spectral behaviour of minerals and rocks for remotely mapping and deriving compositional details about a region.[18,51–56] In the present research work, laboratory spectral measurements were carried out on 12 rock samples collected from the ultramafic terrain of the Sittampundi complex (Figure 2). The rock samples were

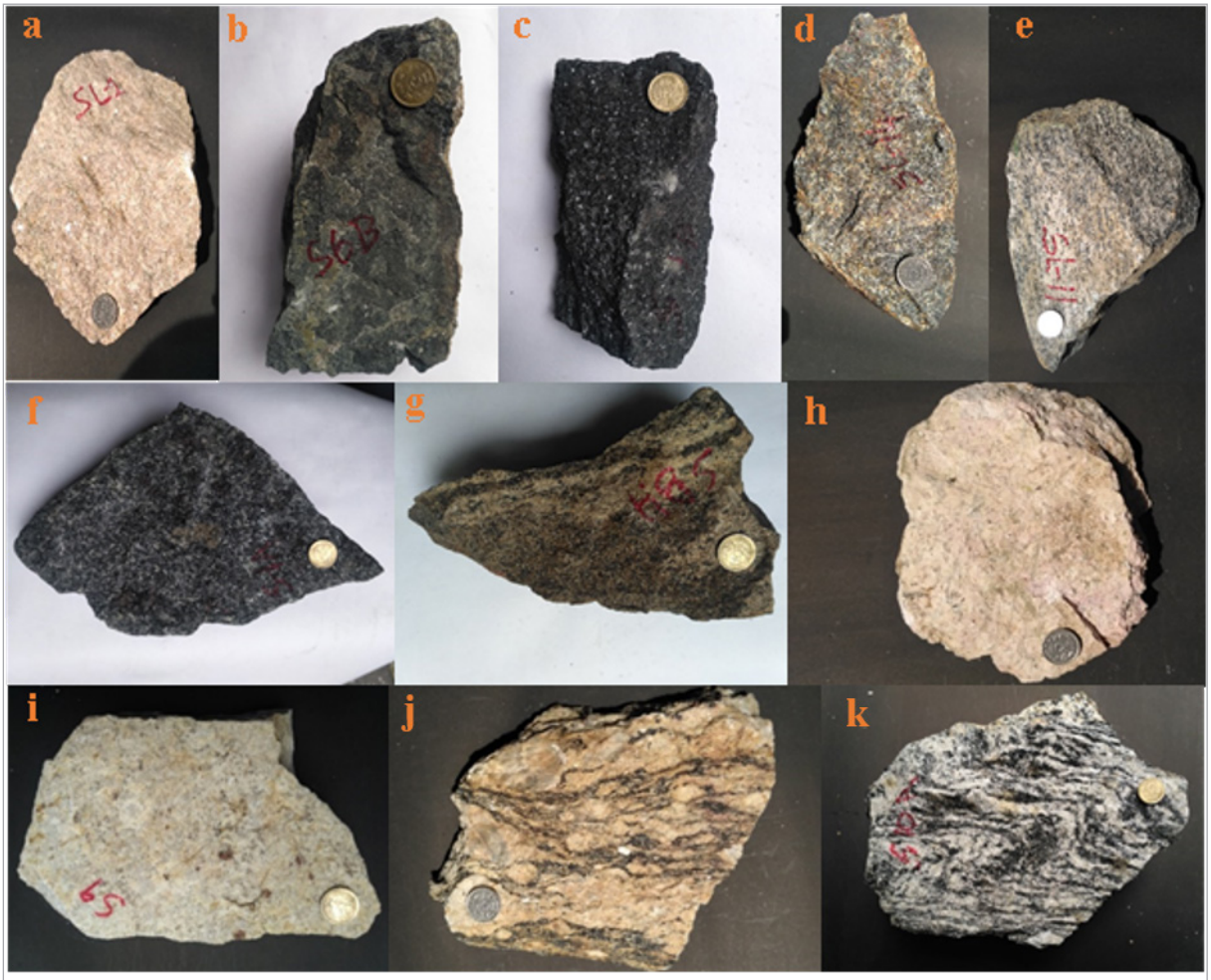

Figure 2. Rock samples collected from Sittampundi ultramafic terrain for mineralogical studies, chemical analysis and spectral measurements. (a) Pink granite, (b) pyroxenite, (c) gabbro, (d) meta-gabbro, (e) anorthosite, (f) pyroxenite, (g) meta-anorthosite, (h) pegmatite, (i) granite, (j) HBG and (k) migmatite.

powdered into 75-µm sizes for spectral measurements. A powdered sample provides increased albedo and depth of absorption bands.[7,57–60] A powder sample provides a better contrasted spectral signature between albedo and absorption bands than a hand specimen. It is easier to use for the extraction of absorption bands from the spectra. Hence, spectral measurements were carried out on the powder sample. The powder samples were prepared from anorthosite, meta-anorthosite, gabbro, meta-gabbro, pyroxenite, gneiss, granite, pegmatite and migmatite rock samples. Reflectance spectral measurements were performed from 350 nm to 2500 nm using an ASD FieldSpec 4 Hi-Res NG field spectroradiometer at IIT Bombay. The spectral measurements were conducted in laboratory conditions using a tungsten lamp as an illumination source. The spectral data were collected at a height of 15 cm from the sample with an instantaneous field of view of 25°. The spectral bandwidth of the instrument is 1.4 nm @ 350–1000 nm and 1.1 nm @ 1001–2500 nm. ENVI 5.3 image processing software was used for processing and plotting of the spectra for various rock types.

AVIRIS-NG data analysis

In the remote sensing era, particularly for the past few decades, hyperspectral remote sensing has provided valuable input for various applications. The hyperspectral sensor is a boon for geoscientists and researchers for lithological mapping, detection and exploration of ores and minerals. Identification of materials or minerals depends upon their spectral resolution, spatial coverage and the signal-to-noise ratio of the spectrometer. In this context, the AVIRIS-NG hyperspectral data were successfully utilised for geological mapping and exploration of potential economic minerals. AVIRIS-NG has 5 nm spectral resolution with a wavelength range of 380–2510 nm.

The specifications of AVIRIS-NG airborne hyperspectral data are given in Table 1.

In the present work, AVIRIS-NG level 2 data were utilised for mapping the ultramafic igneous terrain of the Sittampundi complex. The level-2 data provide atmospherically and radiometrically corrected surface reflectance data. The images were downloaded from the Visualization of Earth Observation Data and Archival System (Vedas) portal of SAC, Ahmedabad (https://vedas.sac.gov.in). The Sittampundi complex is covered under four AVIRIS-NG scenes. The spatial resolution of airborne data ranges from 4 m to 6 m. The AVIRIS-NG data were processed using ENVI 5.3 image processing software. The four scenes of airborne hyperspectral data were merged through mosaicking using a seamless mosaic module available in the software. There are 425 spectral bands in AVIRIS-NG data from 380 nm to 2510 nm. Not all 425 bands in AVIRIS-NG data are required for image processing. Hence, in the next stage, the non-informative bands (noise) were removed and the remaining bands were used for further data analysis. In the level 2 pre-processing stage, 53 bands had already been identified as non-informative bands and removed. The noise bands normally show abnormal reflectance values with a low signal-to-noise ratio. The level-2 data still required removal of a few more noise bands before proceeding with further data analysis. This was done through a visual inspection of the spectral profile. Spectral profiles with abnormal noise level were removed. These particular bands appear completely black or white with uncalibrated output without much information. In this process, an additional 21 noise bands were removed. Out of 425 bands, 74 bands were removed and the remaining 351 bands were used for further image analysis. The AVIRIS-NG False Colour Composite (FCC) image was generated using the B98 (862 nm), B56 (651 nm) and B36 (551 nm) RGB filters (Figure 3). In the image processing technique, generally the FCC image is generated from the NIR (B98), red (B56) and green (B36) bands using RGB filters. The lensoidal shape anorthosite formation (A) is shown as white-bluish in the FCC image. The cultivated land and agricultural plantation (C) areas are shown in red in the central and western parts of the study area. Granite mine (GrM), granitic gneiss (GG) and pink migmatite (PM) could be identified in the FCC image.

Minimum noise fraction

The AVIRIS-NG airborne hyperspectral data has a large volume of data dimensionality, which requires time-consuming computational processes. The minimum noise fraction (MNF) method converts the high-dimensionality data into low-dimensionality data without losing much information. MNF segregates the random noise and reliable data from the signal information. The MNF transform method is more useful for data dimensionality reduction and provides a quality output in the form of transformation image components in a meaningful order.[61] It is referred to as the "whitening" process. The whitening output results in decorrelation and rescaling of noise, which cannot be correlated with any band-to-band combination. In this procedure, the first principal component (PC) transform denotes whitening noise data and the second PC transform generates systematic and non-correlated information in terms of decreasing noise. The remaining 351 AVIRIS-NG bands were used as input data for MNF transformation to obtain a reliable output.

Table 1. Specification of AVIRIS-NG airborne hyperspectral data.

Specification	Value/range	Specification	Value/range
Sensor altitude	4–8 km	Spatial resolution	4–6 m
Swath width	4–6 km	Spatial range	34 ° field of view
Number of bands	425	Spatial sampling	1 mrad
Spectral range	380–2510 nm	Response	1–1.3× sampling
Spectral resolution	5 nm	Sample distance	0.3–20 m
Spectral coverage	Continuous	Geom. model	Full three axes cosines uniformity
Radiometric range	0 to max Lambertian	Spectral cross track	N95 % across FOV
Radiometric precision (SNR)	N2000 @ 600 nm N800 @ 2200 nm	Spectral IFOV variation	N95 % spectral direction
Radiometric accuracy	95 %		

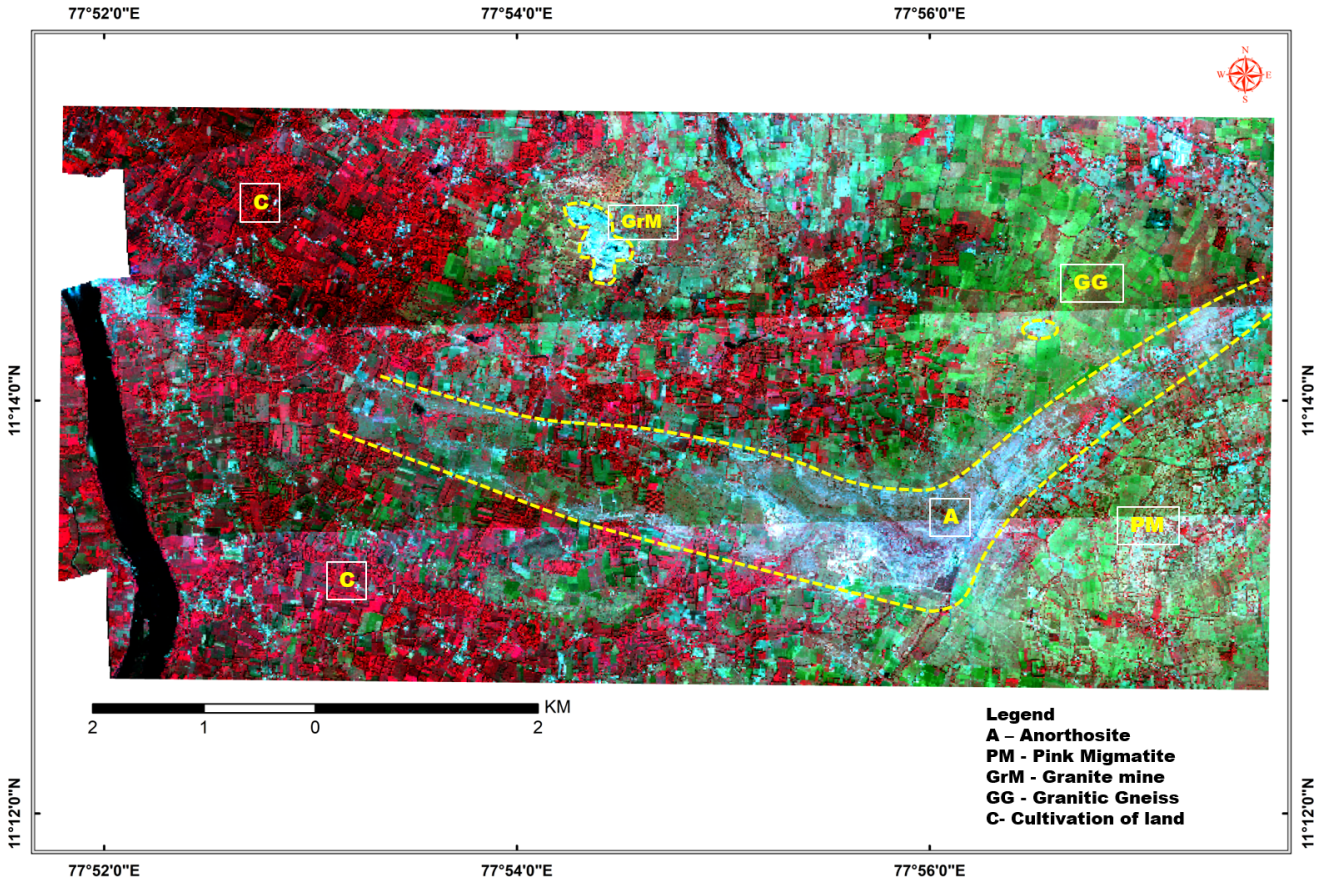

Figure 3. AVIRIS-NG False Colour Composite image generated from B98 (862 nm), B56 (651 nm) and B36 (551 nm) under RGB filters, Sittampundi ultramafic terrain.

The eigenvalues derived from MNF transformation were used for clustering quality band data and noise-dominant datasets. The MNF eigenvalue graph (Figure 4) shows a reliable dataset associated with higher eigenvalues (> 3) and the noise-dominant bands with lesser eigenvalues (< 3). At the end of the MNF transformation, 21 noise-free bands were obtained and considered for further band combination. The 21 MNF bands derived from 351 AVIRIS-NG bands through MNF transformation will not carry wavelength information and they can be referred to only as MNF band 1, MNF band 2 and so on.

Band combination

The MNF transformation provided 21 new sets of MNF bands with low-noise coverage. The new set of MNF bands was used for further image processing and interpretation of various rock types in the ultramafic terrain. The MNF bands 1–17 in the output are noise-free and loaded with good signals. The MNF bands were used for the derivation of various band combinations for the interpretation of various rock types. The band combinations provide enhanced information for lithology and land cover features in a different set of bands in the RGB filters. The various band combination outputs were derived from 17 MNF bands. Out of various combinations, only eight outputs were selected for interpretation based on the clarity and contrast in the image. The selected band combinations B456, B564, B546, B561, B615, B165, B1385 and B8135 are shown as colour composite output.

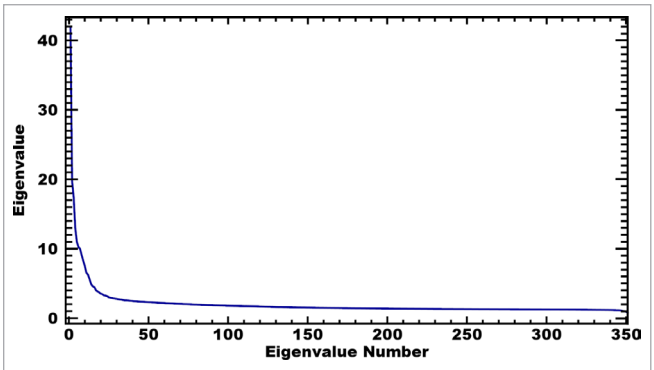

Figure 4. MNF eigenvalue plot show quality band data (value > 3) and noise-dominant bands (value < 3).

Mineralogical studies

The major minerals in the rock samples were identified using petro-thin section studies under a petrological microscope in parallel and crossed polarised conditions. The microscopic thin sections were prepared from anorthosite, meta-anorthosite, gabbro, meta-gabbro, pyroxenite, granite, pegmatite, migmatites and gneissic rock samples.

The major minerals present in anorthosite rock samples are plagioclase and pyroxenes (Figure 5 a and b). The plagioclase minerals show euhedral crystals with polysynthetic twinning. The euhedral to subhedral clinopyroxenes provide 2nd order interference colours and high birefringence with the inclined extension. Similarly, orthopyroxene shows 2nd order interference colours with low birefringence. The pyroxenes show pleochroism under parallel Nicol conditions. The meta-anorthosite in the anorthosite complex represents the presence of plagioclase, pyroxene and, in addition, garnet minerals (Figure 5 c and d). Garnet normally shows euhedral crystal, a light pinkish colour with development of fractures and is isotropic under crossed polarised conditions. Meta-anorthosite also shows sympathetic coronas texture, where the euhedral garnet crystal is surrounded by small anhedral grains of feldspar and pyroxenes. Gabbro and meta-gabbro dominated with clinopyroxene, garnet and feldspar. The gabbro and meta-gabbro show larger crystals of garnet, and finer grains of plagioclase and pyroxene minerals (Figure 5 e–h). The pyroxenite rock sample has varying grain sizes of clino- and orthopyroxene and a lower percentage of plagioclase (Figure 5 i and j). In addition, chromite is also present as an opaque mineral. Light colour minerals such as quartz and orthoclase feldspar are present as major minerals in granite with the absence of mafic minerals. Perthite texture and polysynthetic twinning are commonly present in granite (Figure 5 m and n).

X-ray fluorescence geochemical analysis

In spectral and hyperspectral remote sensing studies, the bulk chemistry of rock types is useful to correlate the spectral behaviour, characterise the spectra and compare with hyperspectral image analysis. Rocks are invariably an aggregate of minerals and provide complicated spectral

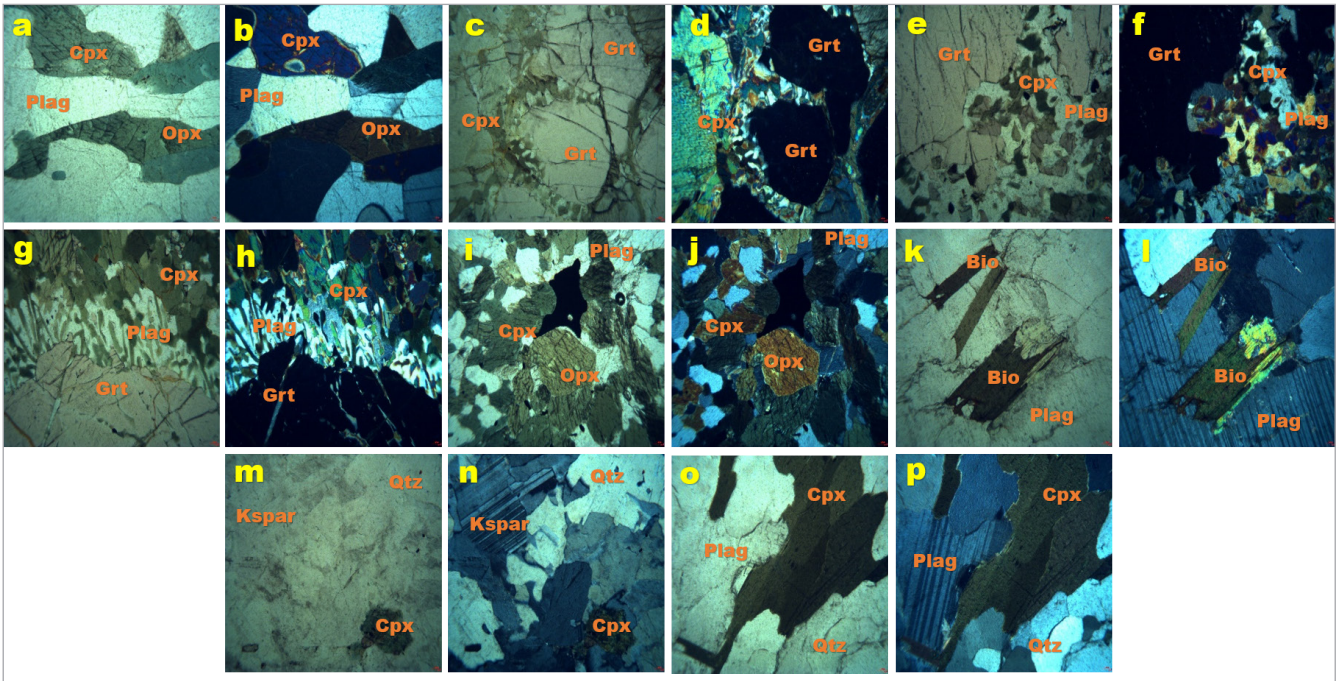

Figure 5. Photomicrograph of rock samples under parallel and crossed Nicol conditions. (a and b) Anorthosite (SiAn1): plagioclase (plag), orthopyroxene (opx) and clinopyroxenes (cpx) in thin section. (c and d) Meta-anorthosite (SiAn4): clinopyroxene (cpx) and garnet (Grt) in the sample. (e and f) Gabbro (SiGb2): clinopyroxene (cpx), plagioclase (plag) and garnet (Grt) in the sample. (g and h) Meta-gabbro (SiMg1): clinopyroxene (cpx), plagioclase (plag) and garnet (Grt) in the sample. (i and j) Pyroxenite (SiPx1): orthopyroxene (opx), clinopyroxene (cpx) and plagioclase (plag) in thin section. (k and l) Pegmatite (SiPt1): plagioclase (plag) and biotite (bio) present in the sample. (m and n) Granite (SiGr1): quartz (qtz), clinopyroxene (cpx) and orthoclase feldspar (Kspar) in the sample. (o and p) Migmatite (SiMt1): quartz (qtz), clinopyroxene (cpx) and plagioclase (plag) in thin section.

signatures. However, we could interpret diagnostic spectral signatures of rocks based on the spectral characteristics of the constituent minerals in the rocks. In this study, the chemistry of 12 rock samples was analysed for the estimation of major oxides. The chemical analysis was carried out with X-ray fluorescence (XRF) using the Rigaku XRF facilities available at IIT Bombay. XRF provides simple, accurate output for the determination of the major elemental composition of rock types. The whole rock powdered samples (75 µm) were utilised for the estimation of major oxides. The major oxides include SiO_2, Al_2O_3, CaO, MgO, Na_2O, K_2O, TiO_2, Fe_2O_3, MnO and P_2O_5. The powder rock samples were converted into pellets for XRF analysis. The sample initially ignited, then fused with lithium tetraborate and the resultant glass disc was irradiated with X-rays. The X-ray photons emitted by the elements in the rock sample were counted and the concentration was determined against the calibrated standards. The major oxides in the rock samples are listed in Table 2.

Results and discussion

The ultramafic terrain of the Sittampundi complex has attracted several geoscientists to study the origin of layered igneous formation, chronology, petrology, chemistry and economic mineral deposits. In the present case, reflectance spectral measurements were carried out along with AVIRIS-NG data analysis, mineralogical studies and chemical analysis. Continuum-removed reflectance spectral data were utilised to interpret the diagnostic spectral features of mafic and ultramafic rocks. The various compositions in the rocks can be dominated by electronic transition processes in the UV-vis-NIR region and vibration processes in the short-wave infrared (SWIR) region.[62] The absorption features associated with the spectral data were interpreted in terms of composition and applied for the discrimination and mapping of rock types.

The reflectance spectra of anorthosite samples obtained from the Sittampundi are mostly featureless in the normal plot with a continuous increase of albedo from visible, NIR to SWIR range. The percentage of reflectance varies from a minimum of 20 % in the visible spectrum to a maximum of 75 % in the SWIR region (Figure 6a). The continuum-removed spectral plot of anorthosites shows diagnostic absorption features in the visible, NIR and SWIR regions. The absorption features of anorthosite in the visible and infrared (IR) spectra are due to electronic processes. The anorthosite spectra also show absorption features due to vibration processes in the SWIR spectrum. The layered igneous complex of Sittampundi anorthosite has undergone several metamorphisms. The metamorphosed anorthosite is referred to as a meta-anorthosite with significant variation in mafic composition and different spectral configurations. The spectral plot of the meta-anorthosite without continuum removal shows an almost similar configuration to the anorthosite. A weak symmetrical absorption noticed at 380 nm and 402 nm in anorthosites (SiAn7, SiAn1, SiAn6) indicated that the electronic transition absorption was due to the presence of ferric iron (Figure 6b). The percentage of ferric iron in the anorthosite ranges from 4.94 % to 5.45 % (Table 2).

Table 2. Major oxides (wt %) in the rock samples collected from Sittampundi ultramafic terrain.

Sample name	Sample ID	SiO_2	TiO_2	Al_2O_3	MnO	Fe_2O_3	MgO	CaO	Na_2O	K_2O	P_2O_5	Total
Anorthosite	SiAn1	41.90	0.11	30.10	0.08	4.94	2.81	18.30	1.42	0.12	0.01	**99.78**
Anorthosite	SiAn6	41.40	0.11	29.40	0.08	5.45	3.39	18.60	1.35	0.03	0.01	**99.84**
Anorthosite	SiAn7	43.50	0.10	29.30	0.08	5.17	3.00	17.20	1.50	0.04	0.01	**99.90**
Meta-anortho	SiAn4	41.00	0.76	16.10	0.30	17.30	8.59	14.50	0.85	0.06	0.11	**99.58**
Gabbro	SiGb2	46.10	1.07	14.40	0.17	14.80	6.43	14.20	2.37	0.14	0.13	**99.81**
Meta-gabbro	SiMg1	45.50	1.05	15.50	0.22	16.70	5.65	12.80	2.03	0.14	0.19	**99.78**
Pyroxenite	SiPx1	46.90	1.21	15.50	0.18	14.40	7.03	9.44	3.17	0.86	0.80	**99.50**
Pyroxenite	SiPx2	42.10	0.81	4.04	0.31	14.10	11.00	26.30	0.61	0.37	0.06	**99.70**
Pegmatite	SiPt1	64.50	—	18.50	—	0.22	0.04	0.28	2.57	13.20	0.24	**99.54**
Pink granite	SiGr1	63.70	0.08	19.20	0.02	1.13	0.28	1.59	7.58	5.60	0.09	**99.26**
HB gneiss	SiHbg3	55.40	1.65	15.50	—	10.30	2.45	4.31	2.73	5.93	0.92	**99.19**
Migmatite	SiMt1	55.10	0.91	16.80	0.13	9.98	5.34	2.73	2.93	5.06	0.18	**99.16**

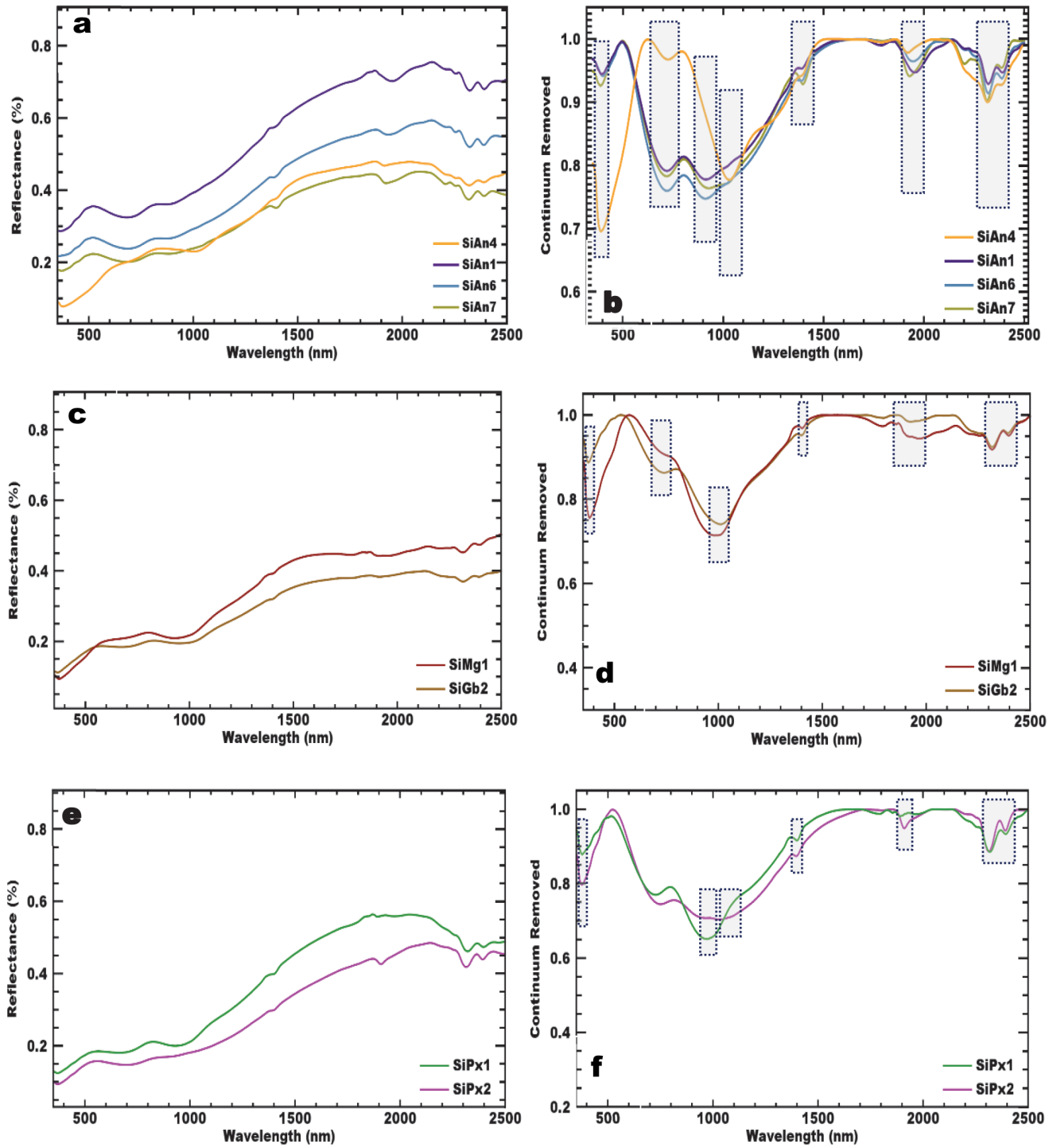

Figure 6. Reflectance spectra of rock samples from ultramafic terrain. (a) Reflectance spectra of anorthosites (SiAn1, SiAn6 and SiAn7) and meta-anorthosite (SiAn4). (b) Continuum-removed reflectance spectra of anorthosites and meta-anorthosite show absorptions at 380 nm, 389–402 nm, 725 nm, 910–925 nm, 1030 nm, 1390–1402 nm, 1915–1956 nm, 2320 nm and 2390 nm. (c) Reflectance spectra of gabbro (SiGb2) and meta-gabbro (SiMg1). (d) Continuum-removed reflectance spectra of gabbro and meta-gabbro show absorptions at 373–380 nm, 737 nm, 994–1011 nm, 1400 nm, 1965 nm, 2317 nm and 2395 nm. (e) Reflectance spectra of pyroxenites (SiPx1 and SiPx2). (f) Continuum-removed spectra of pyroxenites show absorptions at 383 nm, 725 nm, 970 nm,1035 nm, 1400 nm, 1916 nm, 2315 nm and 2395 nm.

In the case of meta-anorthosite, the percentage of iron increased to 17.30 %, and accordingly, it influences the increase of depth of absorption at 389 nm. The continuum-removed meta-anorthosite (SiAn4) shows absorption features at 389 nm, 725 nm, 1030 nm, 1395 nm, 1915 nm, 2320 nm and 2390 nm (Figure 6b). The strong absorption at 389 nm is due to the presence of metal ions of Fe, Cr and Ni. A weak absorption was noticed at 725 nm due to ferric ion electronic transition. Strong pyroxene absorption was seen at 1030 nm due to the presence of high calcic pyroxene minerals. The presence of Mg/OH shows moderate absorption at 2320 nm.

The presence of pyroxene minerals in anorthosites provides diagnostic absorption features between 900 nm and 1000 nm in the IR region.[7] The absorption band centre systematically changes with the composition of iron, magnesium and calcium exchange in pyroxene minerals.[57,63,64] In the present case, the pyroxene mineral (diopside) in the anorthosite influences the absorption band centre. The absorption features in anorthosites were noticed at 910–925 nm due to the low calcic pyroxene mineral. In the case of meta-anorthosite, a strong absorption band centre was seen at 1030 nm, due to the presence of a significant percentage of high calcic pyroxene in the meta-anorthosite. The percentage of iron and magnesium are also comparatively high in meta-anorthosite and it influences the shifting of the absorption band centre more than 1000 nm. The anorthosites with crystalline plagioclase feldspar exhibit broad weak electronic transition absorption near 1200 nm, due to the presence of FeO content of more than 0.1 %.[65–67] In the present case, the reflectance spectra of all four anorthosites show the absence of 1200 nm absorption, which indicates the lack of FeO content in anorthosites. A weak absorption noticed at 1390–1402 nm in the anorthosite indicates the presence of the OH/Mn^{3+} crystal transition process. The moderate symmetrical absorption noticed near 1900 nm (1915–1956 nm) in most of the anorthosite samples reflects the presence of a significant percentage of pyroxene. The absorption doublets observed at 2320 nm and 2390 nm are due to the presence of Mg/OH vibration spectra in anorthosite.

Gabbro is a coarse-grained igneous rock composed of plagioclase and pyroxene minerals. Both clino and ortho pyroxenes are present in gabbro. The mafic elements (Fe, Mg) and pyroxene minerals like diopside and hypersthene are predominant in gabbro, which influences the different spectral behaviour of rocks. The reflectance spectra of both gabbro (SiMg1) and meta-gabbro (SiGb1) show similar spectral signatures with minor variation in albedo (Figure 6 c and d). The percentage of reflectance varies from 10 % to 50 %, which is comparatively lower than the albedo of anorthosite rock samples. The continuum-removed spectra of gabbro and meta-gabbro show moderate symmetrical absorption at 373–380 nm, weak inflection at 737 nm, strong symmetrical absorption at 994–1011 nm, weak inflection at 1400 nm, weak broad absorption at 1965 nm and absorption doublets at 2317 nm and 2395 nm. The significant percentage of ferric iron (14.80–16.70 %) in gabbro and meta-gabbro influences the electronic transition absorption at 373–380 nm and also inflection at 737 nm. The high calcic clinopyroxene (20–28 %) in gabbros provides strong absorptions at 994 nm and 1011 nm. The absorption doublets at 2317 nm and 2395 nm are due to Mg/OH vibration processes.

Pyroxenite is an ultramafic igneous rock, mainly composed of magnesium and iron-rich pyroxene minerals. The reflectance spectra of pyroxenites (SiPx1 and SiPx2) are almost similar to gabbro, except for some variation in absorption band depth. The albedo in the spectra ranges from 10 % to 56 %. The absorption bands are located at 383 nm, 725 nm, 970 nm, 1035 nm, 1400 nm, 1916 nm, 2315 nm and 2395 nm (Figure 6 e and f). The presence of high calcic pyroxene in pyroxenite strongly reflects the symmetrical absorption at 970 nm and broad absorption at 1035 nm. The broad overlapping absorption at 1035 nm is due to the presence of clinopyroxene and olivine in the rock sample.

The layered ultramafic terrain of the Sittampundi Anorthosite Complex is bounded by granite, gneisses, pegmatite and migmatites. Granites are mainly composed of quartz, alkali feldspar and plagioclase minerals. In the study area, pink granites are located in the north of the anorthositic formation, relatively enriched with potassium feldspar. The major country rock that surrounds the ultramafic terrain is gneissic formation. The mafic and felsic minerals equally represented in gneissic rock include quartz, orthoclase, plagioclase, hornblende and other accessory minerals. The spectra of granites (SiGr1) are mostly featureless, however, weak absorptions are noticed at 378 nm, 1421 nm, 1917 nm and 2235 nm, respectively due to ferric iron, crystal transition of OH/Mn^{3+}, ferrous iron/H_2O and Al–OH vibration absorption. The albedo of granite ranges from 35 % to 45 % (Figure 7 a and b). Chemically, granites are dominant with silicates (63 %) and aluminium oxide (19 %). In the study area, pink granites are commercially mined out for decorative stone and building material. Pegmatites are present in between anorthositic layered formations as intrusive rocks. The

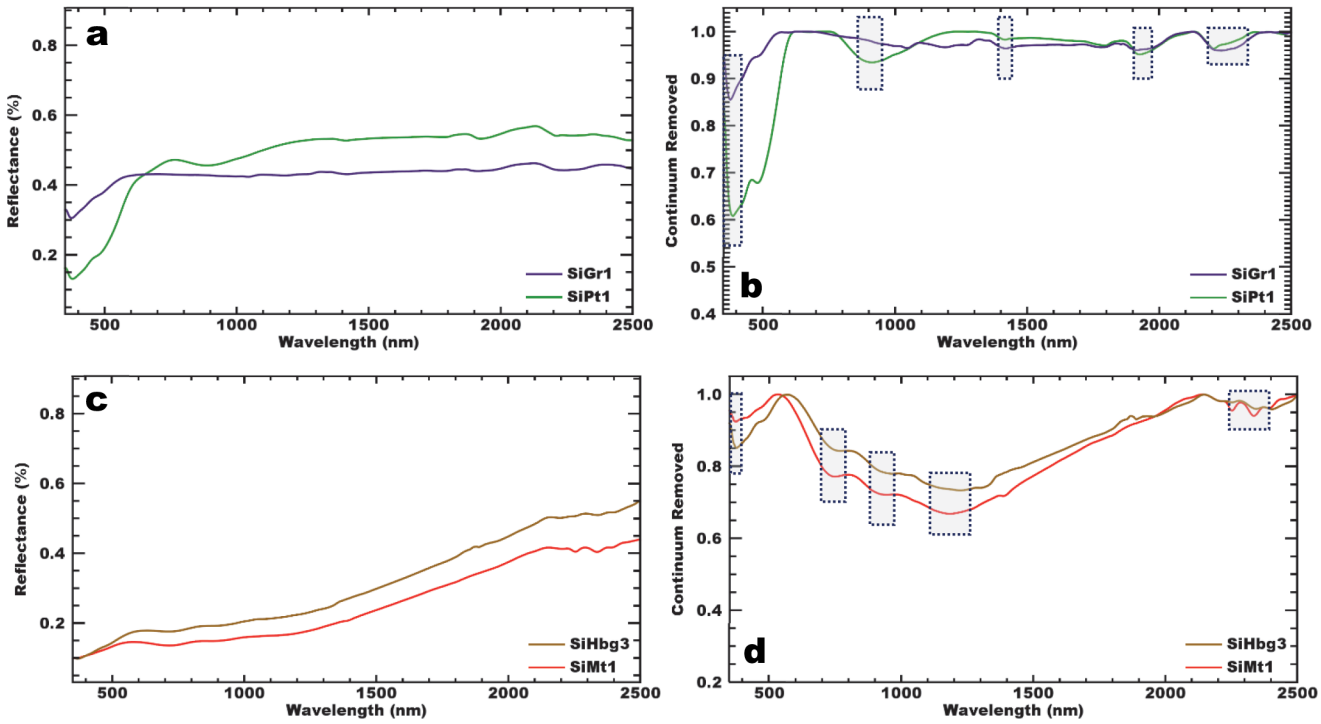

Figure 7. (a) Reflectance spectra of granite and pegmatite (SiGr1 and SiPt1). (b) Continuum-removed reflectance spectra show absorptions at 378 nm, 387 nm, 910 nm, 1421 nm, 1917 nm, 1928 nm, 2208 nm and 2235 nm. (c) Reflectance spectra of HBG and migmatite (SiHbg3 and SiMt1). (d) Continuum-removed reflectance spectra show absorption at 378 nm, 763 nm, 960 nm, 1190–1224 nm, 2255 nm and 2338 nm.

spectra of pegmatite (SiPt1) are almost similar to granites with minor variation in albedo ranging from 15 % to 50 % (Figure 7 a and b). The major minerals present in pegmatite are orthoclase and plagioclase. The chemistry of pegmatite is very close to pink granites in the study area. The absorption bands in pegmatites are strong symmetrical absorption at 387 nm, moderate symmetrical absorption at 910 nm, weak absorptions at 1928 nm and 2208 nm due to ferric iron, low calcic plagioclase, ferrous iron and Al–OH vibration absorptions, respectively.

The metamorphic formation in the study area is quartzo feldspathic hornblende biotite gneiss (SiHbg3), bounded on both sides of the Sittampundi Anorthosite Complex. The gneissic rock contains feldspar, quartz, biotite, hornblende and other mafic accessory minerals. The reflectance spectra of the gneissic rock show a gradual increase of albedo from the visible (10 %) range to the SWIR (55 %) spectrum (Figure 7 c and d). The major oxides in the gneissic rock include SiO_2 (55 %), Al_2O_3 (15 %), Fe_2O_3 (10 %), K_2O (6 %) and CaO (4 %). The continuum-removed spectra of hornblende biotite gneiss show moderate symmetrical absorption at 378 nm, due to the electronic transition of ferric iron. A broad electronic transition absorption band centre was noticed at 1224 nm mainly due to the presence of a significant amount of FeO iron in crystalline plagioclase feldspar. The broad absorption band comprises overlapping absorption centres of ferric iron transition (763 nm) and a low calcic pyroxene absorption band (960 nm) (Figure 7 c and d). The overlapping component can be seen by the inflection at the respective band centre.

The migmatite (SiMt1) rock formation located in the southern part of the anorthosite complex represents high-grade regional metamorphism. The chemistry and mineralogy are very similar to gneissic rock with minor variation in composition, i.e. more felsic rather than mafic content. The spectra of migmatite are also similar to hornblende biotite gneiss with slight variation in albedo (45 %) and absorption depth (Figure 7 c and d). Migmatite also shows moderate absorption at 376 nm, and strong broad overlapping absorption at 1190 nm. In addition, a weak absorption doublet was noticed at 2255 nm and 2338 nm, respectively due to Al–OH and Mg–OH absorptions.

After MNF transformation, 21 MNF bands were obtained for further image processing. Out of 21 bands, 4 MNF bands were selected to delineate rock types in

the Sittampundi igneous complex. The MNF bands 4, 5, 6 and 13 provide enhanced signatures for different lithological formations. MNF B4 significantly enhanced the anorthosite layered formation with a high albedo signature (Figure 8a). The pyroxenite is exposed as a linear grey colour body within the anorthositic layered formation. Similarly, the gabbro/meta-gabbro formation shows an isolated dark colour dull signature within an anorthositic rock formation. MNF B4 also highlighted the granitic mining area with a rectangular bright signature. MNF band 5 provides an excellent boundary condition for anorthositic formation (Figure 8b). This output shows a dark contrast signature for pyroxenite as well as gabbro/meta-gabbro formations. In the south-eastern corner, the PM formation is enhanced and shows clear boundary conditions. The feldspar mine associated with layered igneous formation is also clearly identified in this band with an elevated bright signature. MNF band 6 provides a contrast spectral signature for anorthosite, granites, GG, feldspar mining and migmatites (Figure 9a). It shows reverse spectral signatures for anorthosite formation in a dull pattern along with vegetation coverage. The gabbroic formation shows a smooth grey signature in contrast to the surrounding lithology. The granite and GG show high albedo spectral signatures in the north and north-eastern parts of the study area. MNF band 6 discriminates against built-up areas in the region. MNF B13 shows a contrasting boundary between layered anorthosites and migmatites (Figure 9b). The eastern part of the folded anorthosite formation is exposed with a dark spectral signature. On the other hand, gabbro/meta-gabbro is exposed with a bright spectral signature.

In band combination, the colour composite images were derived from 21 MNF bands. In this process, four composite images were considered for delineating rock types in the ultramafic terrain. The colour composite images include MNF B456, B564, B654 and B561. In these combinations, each image provides a contrast signature for different rock types and is suitable for the interpretation of various lithologies in the study area. The composite image B456 show an excellent signature for almost all rock types including anorthosite (yellow), pyroxenite (orange-red), gabbro (rose red), granite (magenta), migmatite (light green) and GG (blue) (Figure 10a). The MNF band combination B564 provides a clear regional outlook for different rock types (Figure 10b). The band combination of B654 shows a contrast colour signature for anorthosite (A-light blue), pink migmatite gneiss (PM-light green) granite mine (GrM-magenta), granitic gneiss (GG-orange) and hornblende biotite gneiss (HBG) in dark blue to green colour (Figure 11a). At a few locations, the colour overlapping of spectral signatures (colour) was noticed between PM and HBG. It is due to the presence of common minerals like quartz and potash feldspar between the two rock types. MNF B561 composite image is useful in differentiating the lithological boundary between layered anorthosite, GG, migmatites and HBG. The final geological map (Figure 12) was generated for part of the Sittampundi Anorthosite Complex covering mafic and ultramafic igneous rock using the digitally processed AVIRIS-NG airborne hyperspectral data. In this study, the hyperspectral data is useful in the interpretation of gabbro/meta-gabbro and pyroxenite rock bodies within an anorthosite layered formation.

Conclusions

The reflectance spectra of mafic and ultramafic rocks provide a diagnostic spectral signature at various parts of the electromagnetic spectrum. The percentage of albedo, absorption band, type of absorption and absorption depth support the characterisation of the spectra and interpretation of rock types. Most of the rock types have matching absorption bands in the visible, IR and SWIR spectral ranges, however, minor variations like the percentage of albedo, shifting of band centre, overlapping absorption and band depth are useful to differentiate the spectral character in rock-type mapping. The spectral signature of ultramafic rocks differs due to the presence of iron, calcium, magnesium and ferromagnesium minerals, particularly the percentage of different types of pyroxenes.

For example, the strong pyroxene absorption noticed at 990–1000 nm differentiates gabbro from the anorthositic composition. The reflectance spectra of gabbro and pyroxenite are very similar, however, slight variation in the percentage of albedo and band centre occurs depending upon the percentage of pyroxene minerals in pyroxenite. The similarity in composition between gneiss and migmatites reflects a similar spectral signature in the output.

The electronic transition absorption in the visible-IR region and vibration absorption in the SWIR region provide contrast spectral variation at different spectral ranges. The high-resolution AVIRIS-NG airborne hyperspectral image captures this minor spectral variation and supports the interpretation of the various rock types. In this study, the MNF outputs and band combinations are useful in the mapping of different rock types. The

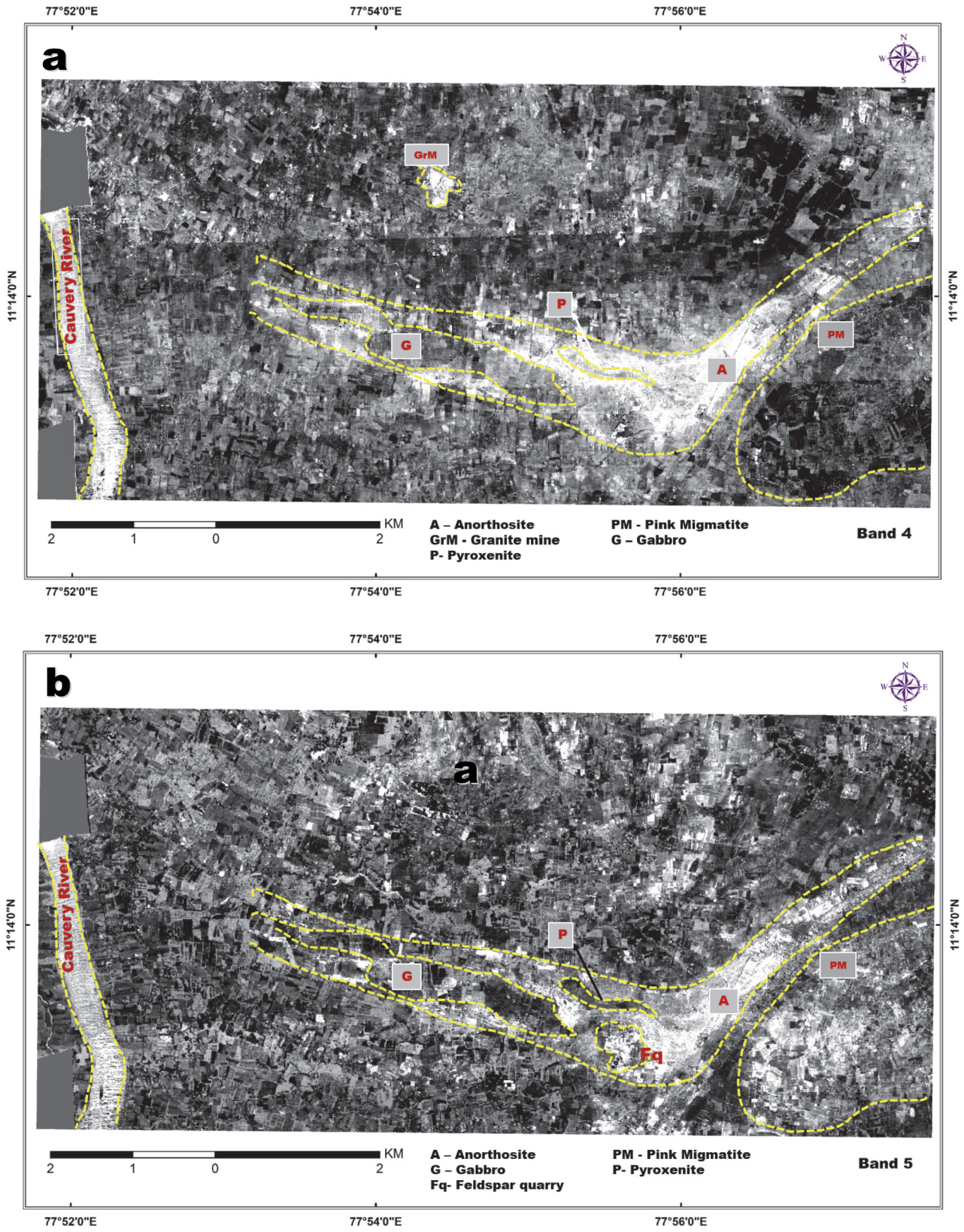

Figure 8. (a) MNF band 4 and (b) MNF band 5 show enhanced output for anorthosite, pyroxenite and gabbro/meta-gabbro.

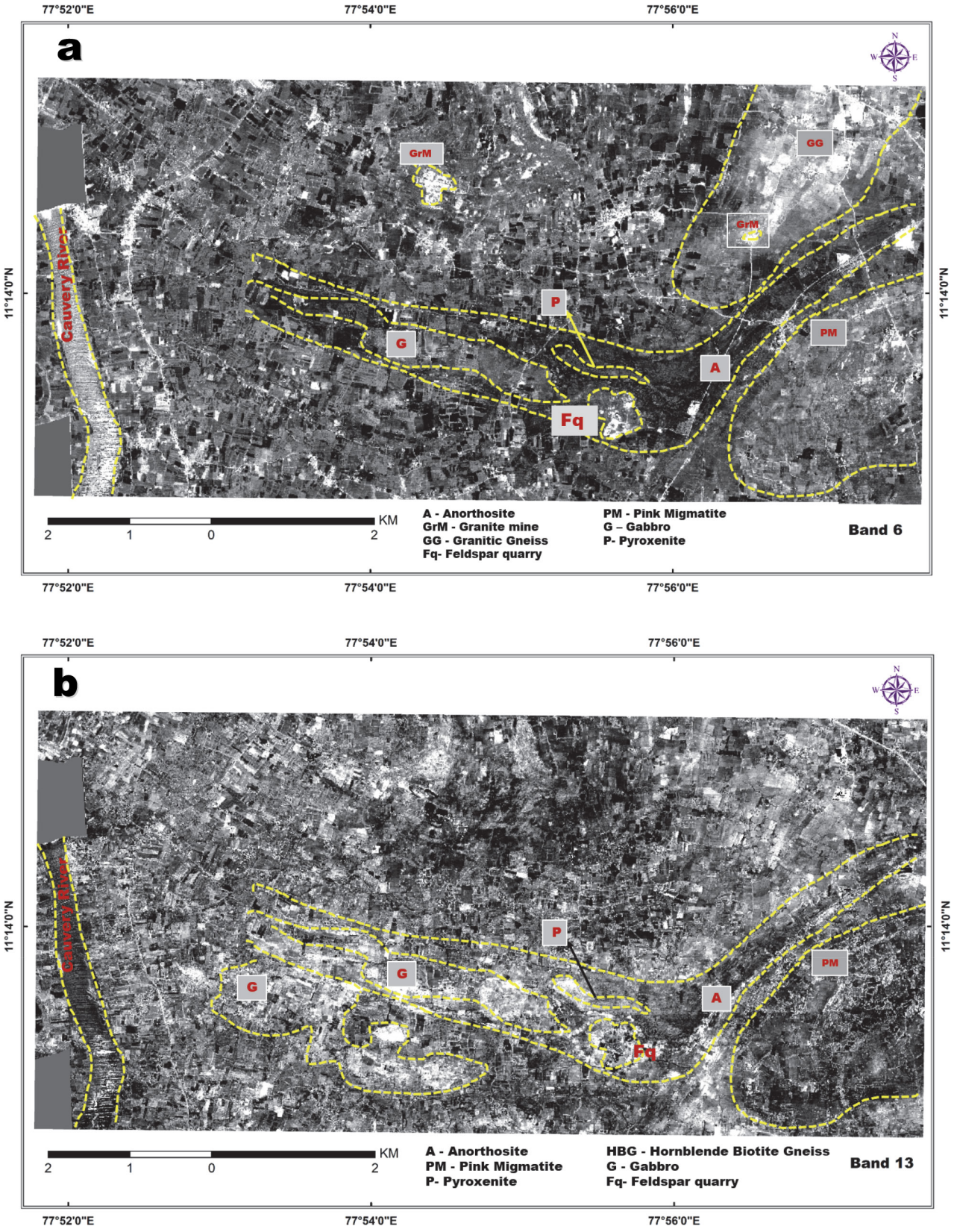

Figure 9. (a) MNF band 6 and (b) MNF band 13 provide contrast signatures for anorthosite, GG, feldspar mining and migmatite.

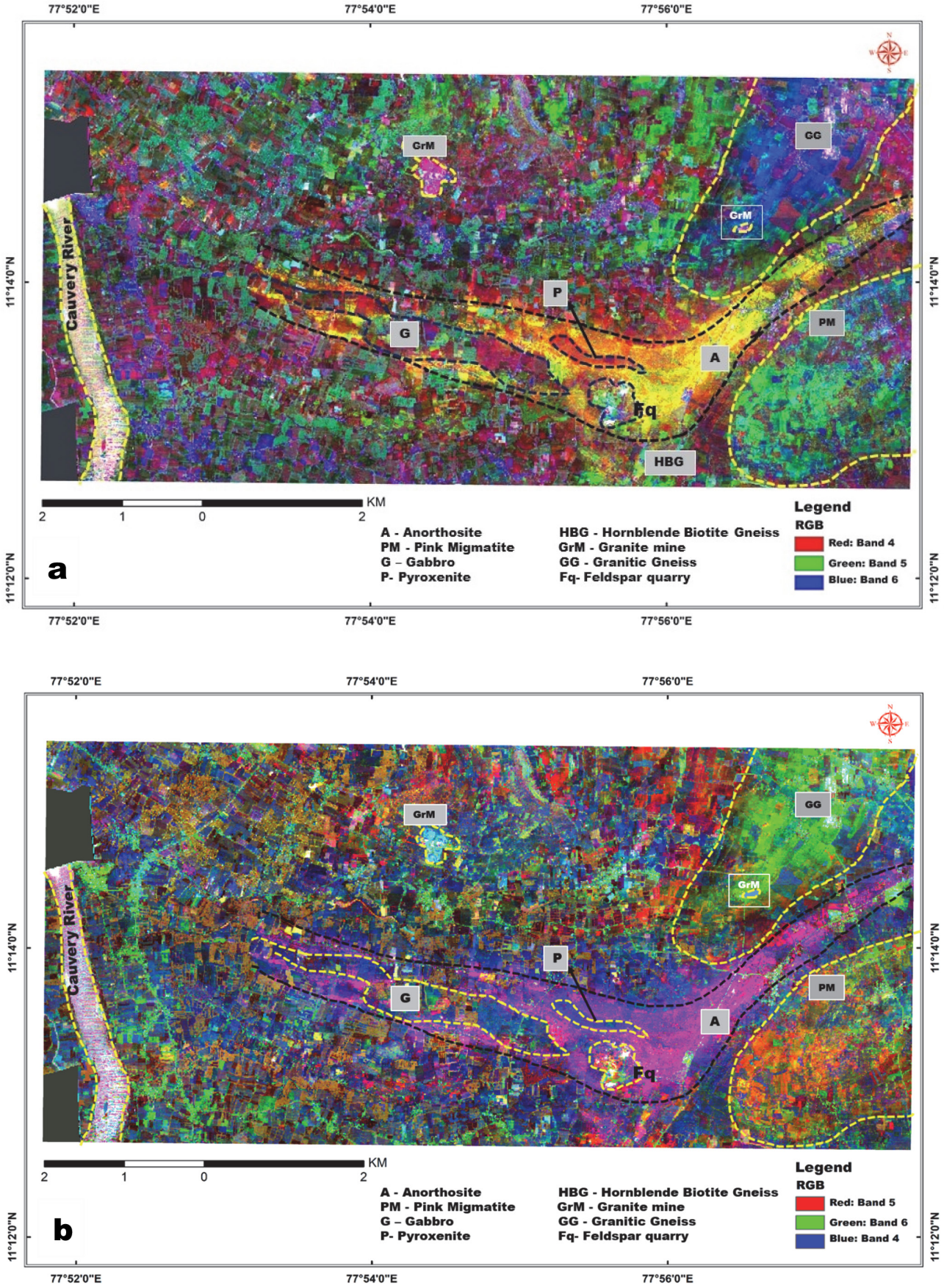

Figure 10. (a) MNF B456 and (b) MNF B564 show contrast signature and regional outlook for different rock types in the ultramafic terrain.

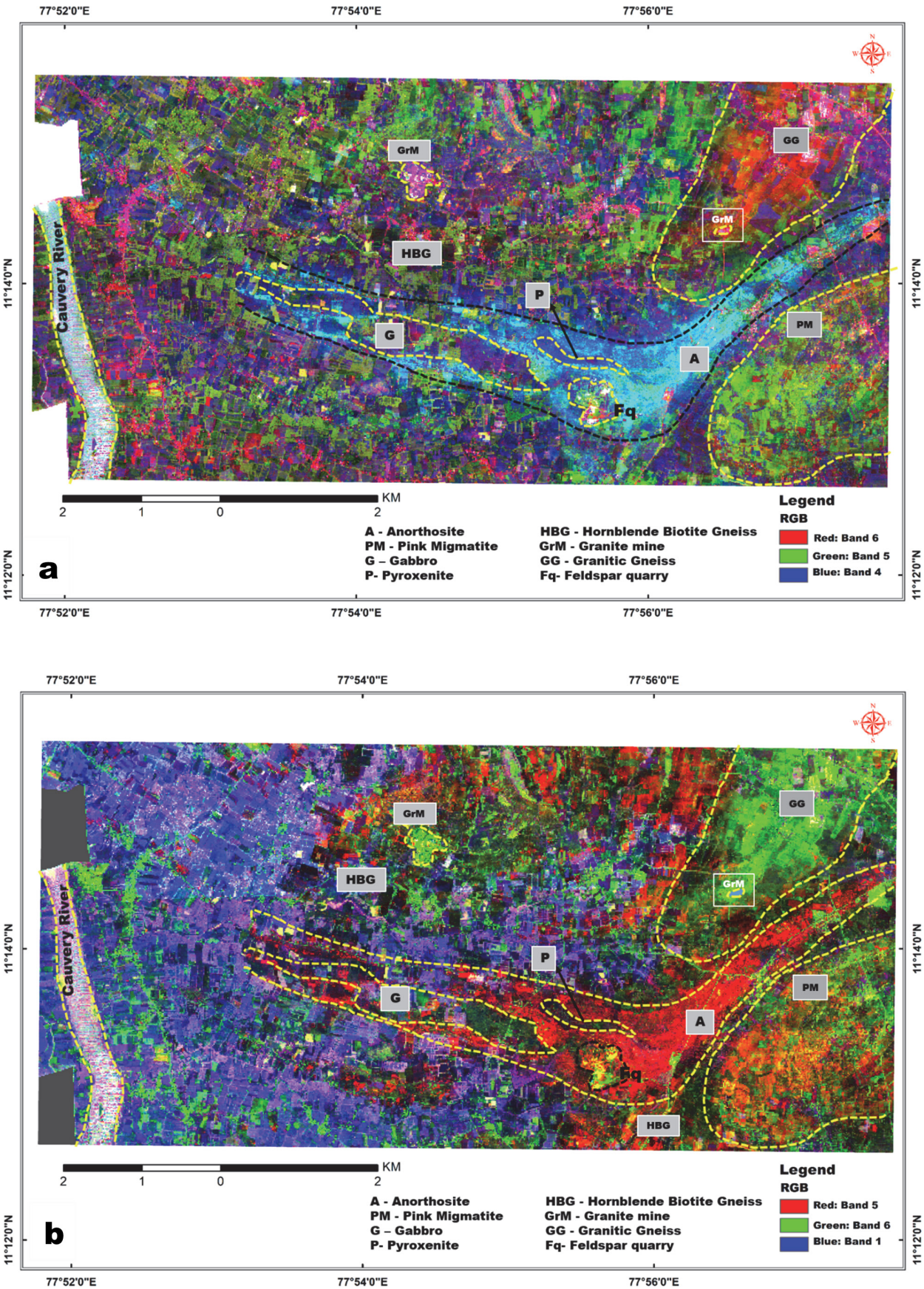

Figure 11. (a) MNF B654 and (b) MNF B561 show contrast signatures for anorthosite, migmatite gneiss, pyroxenite, gabbro, granite mine, GG and HBG.

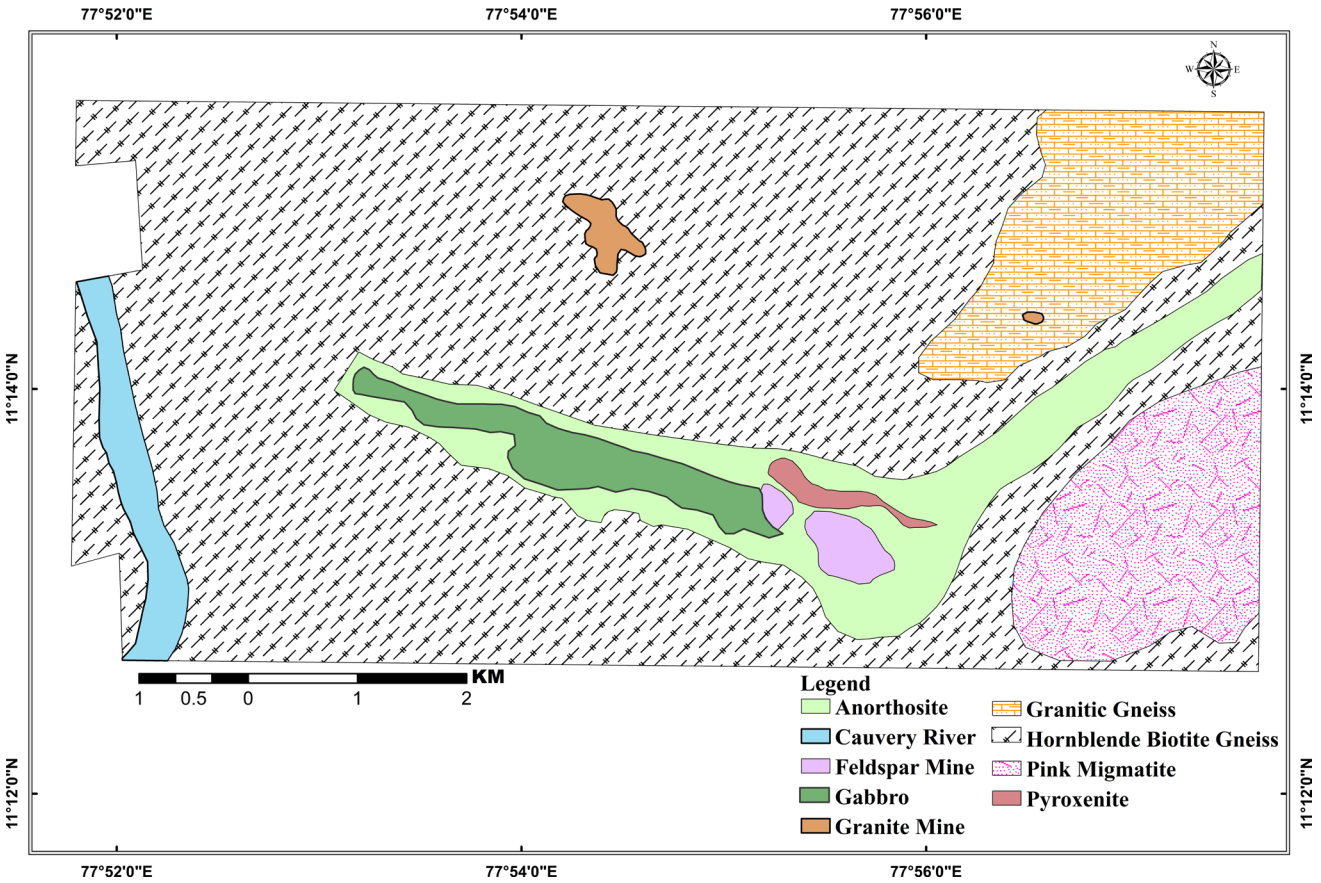

Figure 12. Rock-type mapping prepared from AVIRIS-NG MNF band combination, mainly interpreted from B456 and B654 composite images.

composite image of MNF bands including B456, B546 and B561 is more suitable for the interpretation of rock types and mapping of igneous complex terrain. The band combination supports the preparation of the final geological map for the study area with the inclusion of granites, pyroxenite, gabbro/meta-gabbro and the feldspar mine (pegmatite).

Acknowledgement

The authors thank the Space Application Centre (ISRO), Ahmedabad, for sanctioning the project (Sanction No: EPSA/4.20/2017) under the AVIRIS-NG Announcement opportunity programme.

References

1. F.A. Kruse, "Use of airborne imaging spectrometer data to map minerals associated with hydrothermally altered rocks in the northern grapevine mountains, Nevada, and California", *Remote Sens. Environ.* **24(1),** 31–51 (1988). https://doi.org/10.1016/0034-4257(88)90004-1
2. A.F. Goetz, G. Vane, J.E. Solomon and B.N. Rock, "Imaging spectrometry for Earth remote sensing", *Science* **228(4704),** 1147–1153 (1985). https://doi.org/10.1126/science.228.4704.1147
3. E.A. Cloutis, "Hyperspectral geological remote sensing: Evaluation of analytical techniques", *Int. J. Remote Sens.* **17(12),** 2215–2242 (1996). https://doi.org/10.1080/01431169608948770
4. C.M. Pieters, "Composition of the lunar highland crust from near-infrared spectroscopy", *Rev. Geophys.* **24(3),** 557–578 (1986). https://doi.org/10.1029/RG024i003p00557
5. S. Anbazhagan, I. Venugopal, S. Arivazhagan, M. Chinnamuthu, C.R. Paramasivam, G. Nagesh, S.A. Kannan, Shamarao, V.C. Babu, M. Annadurai, K. Muthukkumaran and V.J. Rajesh, "A lunar soil simulant (LSS-ISAC-1) for the lunar exploration programme of the Indian Space Research

Organisation", *Icarus* **366,** 114511 (2021). https://doi.org/10.1016/j.icarus.2021.114511
6. S. Anbazhagan and S. Arivazhagan, "Reflectance spectra of analog anorthosites: Implications for lunar highland mapping", *Planet. Space Sci.* **58(5),** 752–760 (2010). https://doi.org/10.1016/j.pss.2009.12.002
7. S. Anbazhagan and S. Arivazhagan, "Reflectance spectra of analog basalts; implications for remote sensing of lunar geology", *Planet. Space Sci.* **57(12),** 1346–1358 (2009). https://doi.org/10.1016/j.pss.2009.06.020
8. C.M. Pieters and J.F. Mustard, "Exploration of crustal/mantle material for the earth and moon using reflectance spectroscopy", *Remote Sens. Environ.* **24(1),** 151–178 (1988). https://doi.org/10.1016/0034-4257(88)90010-7
9. F.A. Kruse, A.B. Lefkoff and J.B. Dietz, "Expert system-based mineral mapping in northern death valley, California/Nevada, using the Airborne Visible/Infrared Imaging Spectrometer (AVIRIS)", *Remote Sens. Environ.* **44(2–3),** 309–336 (1993). https://doi.org/10.1016/0034-4257(93)90024-R
10. J.K. Crowley, "Mapping playa evaporite minerals with AVIRIS data: a first report from death valley, California", *Remote Sens Environ.* **44(2–3),** 337–356 (1993). https://doi.org/10.1016/0034-4257(93)90025-S
11. J.W. Boardman and F.A. Kruse, "Automated spectral analysis: A geologic example using AVIRIS data, north Grapevine Mountains, Nevada", *Proceedings, Tenth Thematic Conference on Geologic Remote Sensing*. Environmental Research Institute of Michigan, Ann Arbor, MI, pp. 407–418 (1994).
12. R.N. Clark, G.A. Swayze, L.C. Rowan, K.E. Livo and K. Watson, "Mapping surficial geology, vegetation communities, and environmental materials in our national parks: The USGS imaging spectroscopy integrated geology, ecosystems, and environmental mapping project", *Summaries of the 6th Annual JPL Airborne Earth Science Workshop*, JPL Pub. 96-4, Vol. 1. AVIRIS Workshop, Jet Propulsion Laboratory, California Institute of Technology, Pasadena, CA, pp. 55–56 (1996).
13. J.W. Boardman and J.H. Huntington, "Mineral mapping with 1995 AVIRIS data", *Summaries of the 6th Annual JPL Airborne Earth Science Workshop*, JPL Pub. 96-4, Vol. 1. AVIRIS Workshop, Jet Propulsion Laboratory, California Institute of Technology, Pasadena, CA, pp. 9–11 (1996).
14. J.K. Crowley and D.R. Zimbelman, "Mapping hydrothermally altered rocks on Mount Rainier, Washington, with Airborne Visible/Infrared Imaging Spectrometer (AVIRIS) data", *Geology* **25(6),** 559–562 (1997). https://doi.org/10.1130/0091-7613(1997)025<0559:MHAROM>2.3.CO;2
15. C.R. Paramasivam and S. Anbazhagan, "Application of spectral signature to analyze quality of magnesite ore mineral deposits and altered rocks of Salem, India", *Arab. J. Geosci.* **14,** 651 (2021). https://doi.org/10.1007/s12517-021-06963-1
16. P.M. Thesniya, R. Saranya and V.J. Rajesh, "Compositional and spectrochemical analyses of Cr-spinels in the Sittampundi Anorthosite Complex, Southern India: Implications for remote observation of spinels on the Moon", *Spectrochim. Acta A* **255,** 119677 (2021). https://doi.org/10.1016/j.saa.2021.119677
17. T.V.V. King and R.N. Clark, "Spectral characteristics of chlorites and Mg-serpentines using high-resolution reflectance spectroscopy", *J. Geophys. Res. Solid Earth Planets* **94(B10),** 13997–14008 (1989). https://doi.org/10.1029/JB094iB10p13997
18. R.N. Clark, "Spectroscopy of rocks and minerals, and principles of spectroscopy", *Manual of Remote Sensing*. Wiley, Vol. 3, Ch. 1, pp. 3–58 (1999).
19. R.N. Clark, T.V. King, M. Klejwa, G.A. Swayze and N. Vergo, "High spectral resolution reflectance spectroscopy of minerals", *J. Geophys. Res. Solid Earth* **95(B8),** 12653–12680 (1990). https://doi.org/10.1029/JB095iB08p12653
20. J. Krishnamurthy, "The evaluation of digitally enhanced Indian Remote Sensing Satellite (IRS) data for lithological and structural mapping", *Int. J. Remote Sens.* **18(16),** 3409–3437 (1997). https://doi.org/10.1080/014311697216955
21. R. Pu, *Hyperspectral Remote Sensing: Fundamentals and Practices*. CRC Press, Florida, USA (2017). https://doi.org/10.1201/9781315120607
22. F.A. Kruse, J.W. Boardman and J.F. Huntington, "Comparison of airborne hyperspectral data and EO-1 Hyperion for mineral mapping", *IEEE Trans. Geosci. Remote Sens.* **41(6),** 1388–1400 (2003). https://doi.org/10.1109/TGRS.2003.812908
23. F.A. Kruse, "Advances in hyperspectral remote sensing for geologic mapping and exploration", *9th Australasian Remote Sensing Conference*, Sydney, Australia (1998).

24. F.F. Sabins, "Remote sensing for mineral exploration", *Ore Geol. Rev.* **14(3–4),** 157–183 (1999). https://doi.org/10.1016/S0169-1368(99)00007-4
25. G. Vane and A.F. Goetz, "Terrestrial imaging spectroscopy", *Remote Sens. Environ.* **24(1),** 1–29 (1988). https://doi.org/10.1016/0034-4257(88)90003-X
26. D. Ramakrishnan and R. Bharti, "Hyperspectral remote sensing and geological applications", *Curr. Sci.* **108(5),** 879–891 (2015). https://www.currentscience.ac.in/Volumes/108/05/0879.pdf
27. T. Magendran and S. Sanjeevi, "Hyperion image analysis and linear spectral unmixing to evaluate the grades of iron ores in parts of Noamundi, Eastern India", *Int. J. Appl. Earth Obs. Geoinform.* **26,** 413–426 (2014). https://doi.org/10.1016/j.jag.2013.09.004
28. C.R. Paramasivam and S. Anbazhagan, "Geospatial assessment of ultramafic rocks and ore minerals of Salem, India", *Arab. J. Geosci.* **13,** 1095 (2020). https://doi.org/10.1007/s12517-020-06107-x
29. F.A. Kruse and J.W. Boardman, "Characterization and mapping of kimberlites and related diatremes in Utah, Colorado and Wyoming, USA, using the Airborne Visible/Infrared Imaging Spectrometer (AVIRIS)", *Proceedings 12th Thematic Conference, Applied Geologic Remote Sensing*, 17–19 November 1997, Environmental Research Institute of Michigan (ERIM), Ann Arbor, MI, pp. I-21–I-28 (1997).
30. X. Zhang and M. Pazner, "Comparison of lithologic mapping with ASTER, Hyperion, and ETM data in the southeastern Chocolate Mountains, USA", *Photogramm. Eng. Remote Sens.* **73(5),** 555–561 (2007). https://doi.org/10.14358/PERS.73.5.555
31. M.K. Tripathi and H. Govil, "Evaluation of AVIRIS-NG hyperspectral images for mineral identification and mapping", *Heliyon* **5(11),** e02931 (2019). https://doi.org/10.1016/j.heliyon.2019.e02931
32. M.K. Tripathi, H. Govil and P. Diwan, "Comparative evaluation threshold parameters of Spectral Angle Mapper (SAM) for mapping of Chhabadiya Talc Minerals, Jahajpur, Bhilwara, India using Hyperion hyperspectral remote sensing data", *2019 2nd International Conference on Intelligent Communication and Computational Techniques (ICCT)*, pp. 70–74 (2019). https://doi.org/10.1109/ICCT46177.2019.8969015
33. F.A. Kruse, "Integrated visible and near-infrared, shortwave infrared, and longwave infrared full-range hyperspectral data analysis for geologic mapping", *J. Appl. Remote Sens.* **9(1),** 096005 (2015). https://doi.org/10.1117/1.JRS.9.096005
34. L. Hamlin, R. Green, P. Mouroulis, M. Eastwood, D. Wilson, M. Dudik and C. Paine, "Imaging spectrometer science measurements for terrestrial ecology: AVIRIS and new developments", *2011 Aerospace Conference*, pp. 1–7 (2011). https://doi.org/10.1109/AERO.2011.5747395
35. A.K. Thorpe, C. Frankenberg, A.D. Aubrey, D.A. Roberts, A.A. Nottrott, T.A. Rahn and J.P. McFadden, "Mapping methane concentrations from a controlled release experiment using the next generation airborne visible/infrared imaging spectrometer (AVIRIS-NG)", *Remote Sens. Environ.* **179,** 104–115 (2016). https://doi.org/10.1016/j.rse.2016.03.032
36. T. Oommen and S. Chatterjee, "Mineral potential in India using Airborne Visible/Infrared Imaging Spectrometer-Next Generation (AVIRIS-NG) data", *AGU Fall Meeting Abstracts*, pp. IN43D–0102 (2017).
37. S. Bhattacharya, H. Kumar, A. Guha, A.K. Dagar, S. Pathak, K. Rani, S. Mondal, K.V. Kumar, W. Farr, S. Chatterjee, S. Ravi, A.K. Sharma and A.S. Rajawat, "Potential of airborne hyperspectral data for geo-exploration over parts of different geological/metallogenic provinces in India based on AVIRIS-NG observations", *Curr. Sci.* **116(7),** 1143–1156 (2019). https://doi.org/10.18520/cs/v116/i7/1143-1156
38. A.P. Subramaniam, "Mineralogy and petrology of the Sittampundi complex, Salem district, Madras State, India", *Geol. Soc. Amer. Bull.* **67(3),** 317–390 (1956). https://doi.org/10.1130/0016-7606(1956)67[317:MAPOTS]2.0.CO;2
39. L. Iyer, "On the corundum-bearing rocks of Namakkal taluk, Salem district, Madras Presidency", *Proceeding Indian Science Congress* (1933).
40. S. Ramadurai, M. Sankaran, T. Selvan and B. Windley, "The stratigraphy and structure of the Sittampundi complex, Tamil Nadu, India", *J. Geol. Soc. India* **16(4),** 409–414 (1975).
41. A. Janardhanan and B.E. Leake, "The origin of the meta-anorthositic gabbros and garnetiferous granulites of the Sittampundi complex, Madras, India", *J. Geol. Soc. India* **16(4),** 391–408 (1975).
42. B. Windley and T. Selvan, "Anorthosites and associated rocks of Tamilnadu Southern India", *J. Geol. Soc. India* **16(2),** 209–215 (1975).
43. B.F. Windley, F.C. Bishop and J.S. Smith, "Metamorphosed layered igneous complexes in Archean granulite–gneiss belts", *Ann. Rev.*

Earth Planet. Sci. **9,** 175–198 (1981). https://doi.org/10.1146/annurev.ea.09.050181.001135
44. L.D. Ashwal, *Anorthosites*. Springer-Verlag, p. 421 (2000).
45. S. Mitra, M. Bidyananda and A.K. Samanta, "Cation distribution in Cr-spinels from the Sittampundi layered complex and their intracrystalline thermodynamics", *Curr. Sci.* **90(3),** 435–439 (2006). https://www.currentscience.ac.in/Volumes/90/03/0435.pdf
46. M. Santosh and K. Sajeev, "Anticlockwise evolution of ultrahigh-temperature granulites within continental collision zone in southern India", *Lithos* **92(3–4),** 447–464 (2006). https://doi.org/10.1016/j.lithos.2006.03.063
47. K. Sajeev, B.F. Windley, J.A.D. Connolly and Y. Kon, "Retrogressed eclogite (20 kbar, 1020 °C) from the Neoproterozoic Palghat-Cauvery suture zone, southern India", *Precambrian Res.* **171(1–4),** 23–36 (2009). https://doi.org/10.1016/j.precamres.2009.03.001
48. Y. Rao, T. Chetty, A. Janardhan and K. Gopalan, "Sm-Nd and Rb-Sr ages and PT history of the Archean Sittampundi and Bhavani layered meta-anorthosite complexes in Cauvery shear zone, South India: evidence for Neoproterozoic reworking of Archean crust", *Contrib. Mineral. Petrol.* **125(2),** 237–250 (1996). https://doi.org/10.1007/s004100050219
49. S. Arivazhagan and S. Anbazhagan, "ASTER data analyses for lithological discrimination of Sittampundi Anorthositic Complex, Southern India", *Geosci. Res.* **2(3),** 196–209 (2017). https://doi.org/10.22606/gr.2017.23005
50. *Geological Map of Namakkal District*. Geological Survey of India (GSI) (2005).
51. G.R. Hunt, "Spectral signatures of particulate minerals in the visible and near-infrared", *Geophysics* **42(3),** 501–513 (1977). https://doi.org/10.1190/1.1440721
52. F.D. Van der Meer, H.M. Van der Werff, F.J. Van Ruitenbeek, C.A. Hecker, W.H. Bakker, M.F. Noomen, M. Van Der Meijde, E.J.M. Carranza, J.B. De Smeth and T. Woldai, "Multi-and hyperspectral geologic remote sensing: A review", *Int. J. Appl. Earth Obs. Geoinform.* **14(1),** 112–128 (2012). https://doi.org/10.1016/j.jag.2011.08.002
53. A. Crosta and C. De Souza Filho, "Evaluating AVIRIS hyperspectral remote sensing data for geological mapping in laterized terrains, Central Brazil", *Appl. Geologic. Remote Sens. International Conference*, p. II-430 (1997).
54. S.M. Ramasamy, V. Venkatasubramanian and S. Anbazhagan, "Reflectance spectra of minerals and their discrimination using Thematic Mapper, IRS and SPOT multispectral data", *Int. J. Remote Sens.* **14(16),** 2935–2970 (1993). https://doi.org/10.1080/01431169308904412
55. M. Eismann, *Hyperspectral Remote Sensing*. Society of Photo-Optical Instrumentation Engineers (2012). https://doi.org/10.1117/3.899758
56. Y. Ogen, M. Denk, C. Glaesser, H. Eichstaedt, R. Kahnt, R. Loeser, R. Suppes, M. Chimeddorj, T. Tsedenbaljir and U. Alyeksandr, "Quantification of the spectral variability of ore-bearing granodiorite under supervised and semisupervised conditions: an upscaling approach", *J. Spectrosc.* **2021,** 2580827 (2021). https://doi.org/10.1155/2021/2580827
57. J.B. Adams and A. Filice, "Spectral reflectance 0.4–2.0 mm of silicate rock powders", *J. Geophys. Res.* **72(22),** 5705–5715 (1967). https://doi.org/10.1029/JZ072i022p05705
58. C.M. Pieters, "Strength of mineral absorption features in the transmitted component of near-infrared reflected light: first results from RELAB", *J. Geophys. Res.* **98(B11),** 20817–20824 (1983). https://doi.org/10.1029/JB088iB11p09534
59. E.A. Cloutis and M.J. Gaffey, "Pyroxene spectroscopy revisited: Spectral-compositional correlations and relationship to geothermometry", *J. Geophys. Res. Planets* **96(E5),** 22809–22826 (1991). https://doi.org/10.1029/91JE02512
60. J.M. Sunshine and C.M. Pieters, "Estimating modal abundances from the spectra of natural and laboratory pyroxene mixtures using the modified Gaussian model", *J. Geophys. Res.* **98(E5),** 9075–9087 (1993). https://doi.org/10.1029/93JE00677
61. R.O. Green, G. Vane and J.E. Conel, "Determination of in-flight AVIRIS spectral, radiometric, spatial and signal-to-noise characteristics using atmospheric and surface measurements from the vicinity of the rare-earth-bearing carbonatite at Mountain Pass, California", *Proceedings of the Airborne Visible/Infrared Imaging Spectrometer*, pp. 162–184 (1988).
62. R.P. Gupta, *Remote Sensing Geology*. Springer (2017). https://doi.org/10.1007/978-3-662-55876-8
63. J.B. Adams, "Visible and near-infrared diffuse reflectance spectra of pyroxenes as applied to remote sensing of solid objects in the solar system",

J. Geophys. Res. **79(32),** 4829–4836 (1974). https://doi.org/10.1029/JB079i032p04829
64. R.M. Hazen, P. Bell and H. Mao, "Effects of compositional variation on absorption spectra of lunar pyroxenes", *Lunar and Planetary Science Conference Proceedings*, pp. 2919–2934 (1978).
65. J.B. Adams and L. Goullaud, "Plagioclase feldspars-visible and near-infrared diffuse reflectance spectra as applied to remote sensing", *Lunar and Planetary Science Conference Proceedings*, pp. 2901–2909 (1978).
66. P.M. Bell and H. Mao, "Optical and chemical analysis of iron in Luna 20 plagioclase", *Geochim. Cosmochim. Acta* **37(4),** 755–759 (1973). https://doi.org/10.1016/0016-7037(73)90172-5
67. L. Cheek, C. Pieters, M. Dyar and K. Milam, "Revisiting plagioclase optical properties for lunar exploration", *40th Annual Lunar and Planetary Science Conference*, p. 1928 (2009).